ChemPubSoc Europe

DOI: 10.1002/chem.201703282

CHEMISTRY A European Journal Full Paper

Layered Compounds

Controlled Hydrothermal Crystallization of Anhydrous $Ln_2(OH)_4SO_4$ (Ln = Eu–Lu, Y) as a New Family of Layered Rare Earth Metal Hydroxides

Xuejiao Wang,*[a, b, c, d] Maxim S. Molokeev,[e, f, g] Qi Zhu,[c, d] and Ji-Guang Li*[b, c, d]

Abstract: Anhydrous hydroxide sulfates $Ln_2(OH)_4SO_4$ (Ln = Eu–Lu, Y) were hydrothermally synthesized as a new family of layered rare earth metal hydroxides (LRHs). They crystallize in the monoclinic system (space group *C*2/*m*) with structures built up by alternate stacking of interlayer SO_4^{2-} and the two-dimensional host layer composed of tricapped $[LnO_9]$ trigonal prisms along the *a* axis. In distinct contrast to the recently discovered hydrated LRHs $Ln_2(OH)_4SO_4{\cdot}2H_2O$, which only exist for Ln = La–Dy, the host layers of the anhydrous phase are linked together by sharing edges instead of an O node of the SO_4^{2-} tetrahedron. Rietveld refinement showed that the cell dimension tends to decrease for smaller Ln^{3+}, while the axis angle ($\beta = 98.78$–100.31°) behaves oppositely. Comparative thermogravimetric/differential thermal analysis in air revealed that the dehydroxylation and desulfurization temperatures become gradually higher and lower, respectively, for smaller Ln^{3+}, and thus the temperature range of $Ln_2O_2SO_4$ existence is narrowed. The newly discovered $Ln_2(OH)_4SO_4$, together with their hydrated counterparts, allow for the first time green synthesis of $Ln_2O_2SO_4$ with water as the only exhaust for the full spectrum of lanthanides. Calcining $Ln_2(OH)_4SO_4$ in H_2 yielded phase-pure Ln_2O_2S for Eu and Gd and a mixture of Ln_2O_2S and Ln_2O_3 for the other Ln. The effects of the lanthanide contraction were clearly revealed, and photoluminescence was found for the anhydrous LRHs of Eu and Tb.

Introduction

Layered inorganic compounds have found broad applications in the fields of drug delivery,[1] catalysis,[2] high-performance microelectronics,[3] flame retardants,[4] hydrogels,[5] UV shielding,[6] and luminescence.[7] Layered rare earth metal hydroxides (LRHs) beneficially combine a layered crystal structure and the abundant and unique optical, magnetic, and catalytic functionalities of the rare earth elements, and are thus of great research interest.[8–11] This group of layered compounds has the general formula $Ln_2(OH)_{6-m}(A^{x-})_{m/x}{\cdot}nH_2O$, where Ln is a trivalent rare earth metal ion, A is a guest anion, $1.0 \le m \le 2.0$, and $n =$ 0–2. Studies on LRHs can be dated back to the late 1960s and are exemplified by the work on $Ln(OH)_2A$ ($A = Cl^-$ or NO_3^-), which consists of alternating hydrogen-bonded $[Ln(OH)_2]^+$ and A^- layers.[12,13] LRHs have gained new attention since Gándara et al. reported in 2006 that the layered metal–organic frameworks $[Ln_4(OH)_{10}(H_2O)_4]_nA_n$ (Ln = Ho, Dy, Yb, Y; A = organic anion) can be superior heterogeneous catalysts because of their ability to facilely vary their coordination number in the catalysis process.[8] Subsequent efforts in synthesis,[14,15] interlayer exploration,[16,17] and structure characterization[18–20] have identified that the $Ln_2(OH)_5A{\cdot}1.5H_2O$ family (A = halide, NO_3^-; $m = 1$, $x = 1$, and $n \approx 1.5$ in the general formula) is generally capable of facile anion exchange and intercalation, and since then exfoliation of $Ln_2(OH)_5A{\cdot}1.5H_2O$ crystals into nanosheets[21,22] and further functionalization with either the pristine crystallites or exfoliated nanosheets has been achieved.[23–25] This group of LRH is more readily crystallized for the intermediate-sized Ln^{3+} (Ln = Sm–Tm, Y) by the well-established synthetic strategies of refluxing (homogeneous precipitation),[18,26] hydrothermal reaction,[27] and controlled titration.[15] The LRHs of the larger La^{3+} and Nd^{3+} were obtained by Byeon et al. by sol-

[a] Dr. X. Wang
College of New Energy, Bohai University
New Songshan District, Jinzhou, Liaoning, 121013 (P. R. China)
E-mail: wangxuejiao@bhu.edu.cn

[b] Dr. X. Wang, Prof. Dr. J.-G. Li
Research Center for Functional Materials
National Institute for Materials Science
Tsukuba, Ibaraki 305-0044 (Japan)
E-mail: Li.jiguang@nims.go.jp

[c] Dr. X. Wang, Dr. Q. Zhu, Prof. Dr. J.-G. Li
Key Laboratory for Anisotropy and Texture of Materials
(Ministry of Education), Northeastern University
Shenyang, Liaoning 110819 (P. R. China)

[d] Dr. X. Wang, Dr. Q. Zhu, Prof. Dr. J.-G. Li
Institute of Ceramics and Powder Metallurgy
School of Materials Science and Engineering, Northeastern University
Shenyang, Liaoning 110819 (P. R. China)

[e] Dr. M. S. Molokeev
Laboratory of Crystal Physics, Kirensky Institute of Physics
Federal Research Center KSC SB RAS, Krasnoyarsk 660036 (Russia)

[f] Dr. M. S. Molokeev
Department of Physics, Far Eastern State Transport University
Khabarovsk 680021 (Russia)

[g] Dr. M. S. Molokeev
Siberian Federal University, Krasnoyarsk 660041 (Russia)

Supporting information and the ORCID identification number(s) for the author(s) of this article can be found under https://doi.org/10.1002/chem.201703282.

vothermal reaction of the corresponding nitrate and MOH (M = K, Rb, Cs) in ethanol, and their ability to undergo anion exchange and exfoliation was also demonstrated.[28] For the second smallest lanthanide ion Yb^{3+}, Fogg et al. found that the product tends to be a mixture of the three layered phases of $Yb_2(OH)_5NO_3{\cdot}nH_2O$, where $n = 1.0$, 1.5, and 2.0, and the anion-exchangeable $Yb_2(OH)_5NO_3{\cdot}1.5H_2O$ was isolated by applying kinetic control.[10] For the smallest cation Lu^{3+}, a phase-pure LRH has not been reported to the best of our knowledge.

The sulfate-type LRHs $Ln_2(OH)_4SO_4{\cdot}2H_2O$ ($A = SO_4^{2-}$; $m = 2$, $x = 2$, and $n \approx 2$ in the general formula) were synthesized by Sasaki et al. in 2010 by heating to reflux a solution of $Ln_2(SO_4)_3{\cdot}8H_2O$, Na_2SO_4, and hexamethylenetetramine (homogenous precipitation),[29] and their crystal structure was subsequently studied in detail.[30,31] This new category of LRHs distinguishes itself from the $Ln_2(OH)_5A{\cdot}1.5H_2O$ family in that its hydroxide host layers exclusively consist of LnO_9 polyhedra, with the interlayer SO_4^{2-} coordinated to the Ln center in a bidentate fashion (non-exchangeable), while those of $Ln_2(OH)_5A{\cdot}1.5H_2O$ are constructed by edge sharing of LnO_8 ($[Ln(OH)_7H_2O]$) and LnO_9 ($[Ln(OH)_8H_2O]$) polyhedra, with free interlayer anions for charge compensation.[15,27,32,33] From the viewpoint of chemical composition, a unique feature of $Ln_2(OH)_4SO_4{\cdot}2H_2O$ is that it has exactly the same Ln/S molar ratio as the rare earth metal oxide sulfates ($Ln_2O_2SO_4$) and oxide sulfides (Ln_2O_2S), two important groups of compounds that have diverse functionalities. For example, Ln_2O_2S is well known as a host lattice for efficient luminescence and is widely used in the fields of UV light-emitting diodes, persistent luminescence, cathode-ray tubes, plasma display panels, and X-ray computed tomography.[34–37] $Ln_2O_2SO_4$ can act as precursor for the fabrication of Ln_2O_2S and itself has promising applications in oxygen storage, catalysis, and luminescence.[38–41] The traditional synthesis of $Ln_2O_2SO_4$ and Ln_2O_2S is generally independent of harmful reactants/exhausts such as elemental sulfur, $Na_2S_2O_3$, H_2S, CS_2, and SO*x*. In this regard, $Ln_2(OH)_4SO_4{\cdot}2H_2O$ is an ideal precursor, since its unique Ln/S molar ratio allows simple dehydration and dehydroxylation of this type of LRH under appropriate annealing to yield $Ln_2O_2SO_4$ and Ln_2O_2S with water as the only byproduct.[29,31,42]

Sulfate-type LRH seem to be limited to the larger lanthanide ions Pr–Tb by the aforementioned homogeneous precipitation technique.[29] We recently synthesized $Ln_2(OH)_4SO_4{\cdot}2H_2O$ by hydrothermal reaction of Ln nitrate and ammonium sulfate, and thus extended the family to Ln = La–Dy (excluding Ce and Pm).[42] In our further efforts to expand the sulfate family of LRH compounds, we identified the anhydrous hydroxide sulfate $Ln_2(OH)_4SO_4$ as a new type of LRH for the smaller lanthanide ions Eu–Lu (including Y). This newly discovered group of LRHs, together with the hydrated $Ln_2(OH)_4SO_4{\cdot}2H_2O$ reported recently, allows the green synthesis of $Ln_2O_2SO_4$ for the whole lanthanide series (including Y) and also provides an opportunity to explore the effects of the lanthanide contraction on the structural features and stability of $Ln_2O_2SO_4$ and Ln_2O_2S. Herein, we report the selective crystallization, crystal structure, and thermolysis of $Ln_2(OH)_4SO_4$ as well as the phase transition on calcination. The photoluminescence properties were studied for the anhydrous LRHs of Eu and Tb.

Results and Discussion

Characterization and structure analysis of $Gd_2(OH)_4SO_4$

Hydrothermal reaction of a turbid solution containing $Gd(NO_3)_3$, $(NH_4)_2SO_4$, and $NH_3{\cdot}H_2O$ at 150 °C and pH 10 produced a white precipitate. XRD analysis yielded sharp and symmetric reflections indicating a highly crystalline product (Figure 1a). Elemental analysis of the same product found 66.6 wt% Gd, 6.90 wt% S, 0.01 wt% N, and 0.06 wt% C, from which the chemical formula $Gd_2(OH)_{3.91}(SO_4)_{1.01}(NO_3)_{0.003}(CO_3)_{0.02}$ can be derived if one assumes that the trace amounts of N

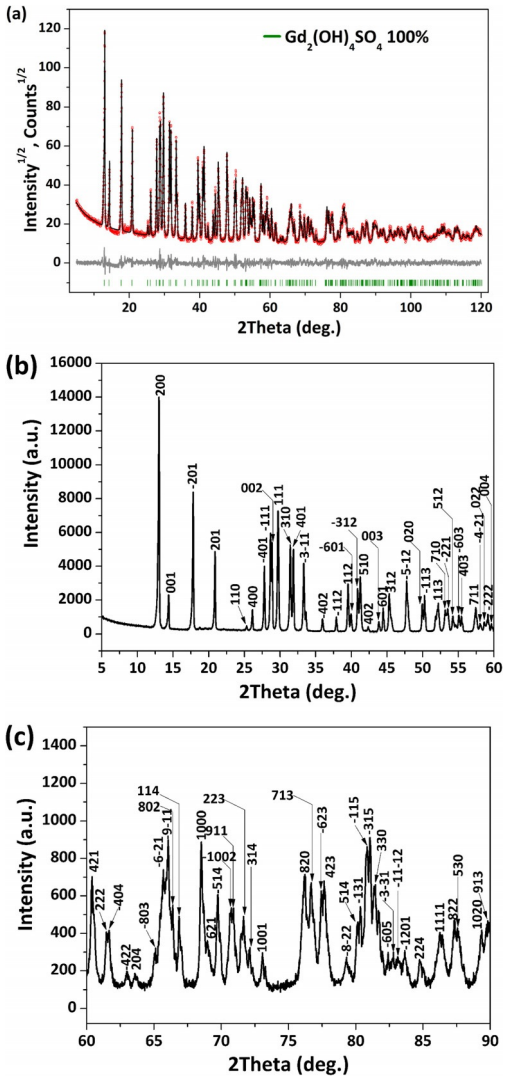

Figure 1. Final Rietveld difference plot of $Gd_2(OH)_4SO_4$, obtained by hydrothermal reaction at 150 °C and pH 10 (a), and indexing of the diffraction peaks in the 2θ ranges of 5–60° (b) and 60–90° (c). In (a), the observed pattern is shown by the black solid line, the calculated data are shown by the red dots, the positions of Bragg reflections are indicated by the green tick marks, and the difference between the results of experiment and calculation is given by the gray line.

and C solely came from contamination with NO_3^- (from Gd nitrate) and CO_3^{2-} (from dissolved atmospheric CO_2). The product can accordingly be approximated as $Gd_2(OH)_4SO_4$. This composition is identical to that of the recently reported LRH $Gd_2(OH)_4SO_4{\cdot}2H_2O$,[29,42] except that it does not contain any water of hydration. The absence of water of crystallization was further confirmed by comparing the FTIR spectra of this new compound and $Ln_2(OH)_4SO_4{\cdot}2H_2O$ (Figure S1, Supporting Information), which clearly show that they both contain hydroxyl groups and SO_4^{2-}, but the former lacks the O–H stretching (ν_1 and ν_3, $\approx$3219 cm^{-1}) and H-O-H bending (ν_2, $\approx$1676 cm^{-1}) vibrations of water of hydration.

All of the XRD peaks of $Gd_2(OH)_4SO_4$ can be indexed to the *C*-centered monoclinic cell, and further analysis of reflection extinctions showed that the most probable space group is *C*2/*m*. To establish the crystal structure a simulated annealing procedure was applied to the randomized coordinates of one Gd, one S, and four O ions.[43] Eighteen varied parameters were obtained, indicating the rationality and high degree of success of the proposed crystal structure. The dynamical occupancy correction of the atoms was used to merge the ions lying on a special position.[44–46] After the calculations, a solution was found with acceptable *R* factors (Table 1). The proposed crystal structure contains one SO_4^{2-} tetrahedron disordered between two positions like in the hydrated LRHs $Ln_2(OH)_4SO_4{\cdot}2H_2O$,[29,30] and the LnO_9 polyhedron is in the form of tricapped trigonal prism with one O node disordered between two positions (Figure 2). Hydrogen atoms were not localized in the difference electron-density map and their positions could not be derived from the analysis of probable hydrogen bonds, and therefore they were omitted from the crystal structure. Refinement of this model is stable and gives acceptable *R* factors (Table 1). The fractional atomic coordinates, isotropic displacement parameters, atomic occupancy, Wyckoff sites (W) and bond valence sums (BVS) are listed in Table 2, and the main bond lengths of the structure can be found in Table S1 of the Supporting Information. The BVS for each ion in the structure was calculated by using the constants from refs. [47,48] and taking into account the fractional occupancies of all the ions (Table 2). These values are close to the valences of Gd^{3+}, S^{6+}, $(OH)^-$, and O^{2-} ions, respectively. The total sum of all the BVS in the unit cell, calculated with the equation $BVS_{total} = \Sigma[(occ)_i{\cdot}(W)_i{\cdot}BVS_i]$, where *i* is the number of specific ions, is 0.105 and thus quite close to 0. Structural analysis of $Gd_2(OH)_4SO_4$ with the program PLATON[49] did not reveal additional elements of symmetry, which further confirms the suggested *C*2/*m* space group. The diffraction peaks in Figure 1b,c were thus indexed according to the results of the Rietveld refinement.

Table 1. Results of structure refinements for the anhydrous hydroxyl sulfate compound $Gd_2(OH)_4SO_4$

Space group	Cell parameters	R_{wp}, R_p [%], χ^2	R_B [%]
*C*2/*m*	a = 13.8759(5) Å b = 3.6577(1) Å c = 6.2842(2) Å β = 99.057(1)° V = 314.97(2) Å^3	9.31, 4.70, 1.98	2.95

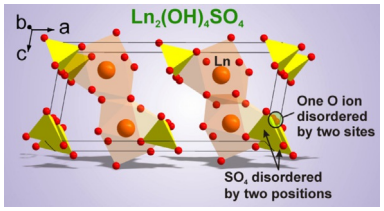

Figure 2. Schematic illustration of the crystal structure of $Gd_2(OH)_4SO_4$.

Table 2. Fractional atomic coordinates, isotropic displacement parameters B_{iso} [Å^2], atomic occupancy (Occ.), Wyckoff sites (W), and bond valence sums (BVS) of $Gd_2(OH)_4SO_4$.

	x	*y*	*z*	B_{iso}	Occ.	W	BVS
Gd	0.19468 (7)	0.5	0.2303 (2)	0.95 (8)	1	4i	2.98
S	0.5006 (7)	0.5	0.131 (1)	1.5 (2)	0.5	4i	6.33
O_{1h}	0.1690 (6)	0	0.480 (2)	2.0 (3)	1	4i	−0.97
O_{2h}	0.2938 (6)	0	0.152 (1)	2.0 (3)	1	4i	−1.11
O_3	0.5869 (7)	0.5	0.049 (2)	3.3 (3)	1	4i	−2.23
O_4	0.5021 (7)	0.188 (3)	0.723 (1)	2.3 (3)	0.5	8j	−1.73

Figure 2 shows the solved crystal structure of anhydrous $Gd_2(OH)_4SO_4$ (space group *C*2/*m*), which can be viewed as an alternate stacking of the sulfate anions and hydroxide main layers, composed of [GdO_9] polyhedra, along the *a* axis. Among the nine O atoms coordinated to each Gd center, six stem from hydroxyl groups and three from the SO_4^{2-} tetrahedron, and the [GdO_9] polyhedron is a tricapped trigonal prism. Each unit cell contains four Gd atoms, and thus the structural composition can be expressed as $Gd_4(OH)_8(SO_4)_2$. The circle in Figure 2 indicates that one O ion is disordered over two sites (one O ion distributed over these two sites). The reason for such a behavior is that these two sites have the same potential energy and a small potential barrier, which allows the O ion to easily jump from one site to another, as shown in Figure S2 of the Supporting Information. Averaging over time and space leads to "two sites" occupied by one O ion with occupancy of 1/2 for each. This can be understood as 1) one O ion jumping from one site to another site (disordering over time), and 2) one O ion being located in a first site in one unit cell, while another O ion is located in a second site in another unit cell (disordering over space). Though it cannot be credibly decided which type of disorder occurs in the structure, such disorder usually occurs in structures with large voids in which the ion can easily migrate.

Figure 3 compares the stacking and coordination modes of anhydrous $Gd_2(OH)_4SO_4$ (Figure 3b) and its hydrated $Gd_2(OH)_4SO_4{\cdot}2H_2O$[42] counterpart (Figure 3a). The two structures share similarities in that the Gd-containing main layer and interlayer SO_4^{2-} anions stack along the *a* axis and that the host layer solely consists of [GdO_9] polyhedra. Note that Figure 3b shows a coordination number (CN) of ten because a static averaged structure was given for the disordered O atom (O_4), as discussed above. Despite the above structural similarities, the anhydrous LRH $Gd_2(OH)_4SO_4$ distinguishes itself from

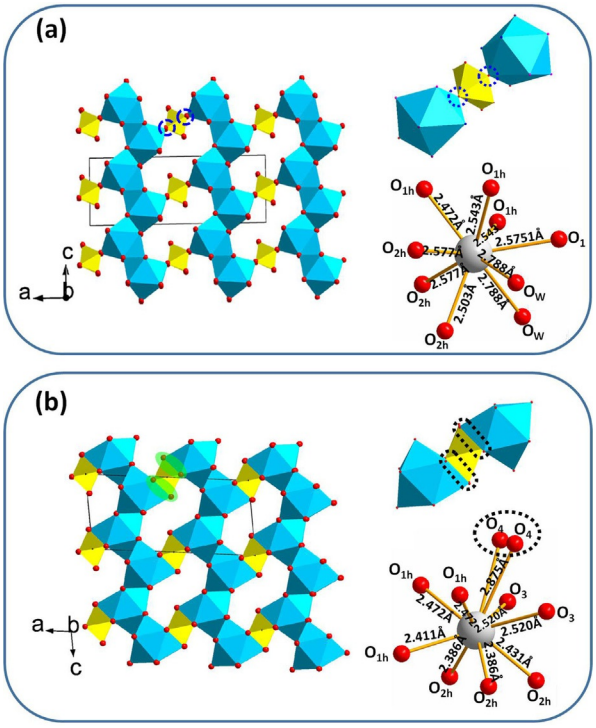

Figure 3. Comparison of the crystal structures of $Gd_2(OH)_4SO_4{\cdot}2H_2O$ (a) and $Gd_2(OH)_4SO_4$ (b).

$Gd_2(OH)_4SO_4{\cdot}2H_2O$ in that: 1) the hydroxide main layers are linked with the interlayer anions through sharing edges (Figure 3b) rather than O nodes (Figure 3a) of the sulfate tetrahedron; 2) in $Gd_2(OH)_4SO_4{\cdot}2H_2O$, among the nine O atoms coordinated to each Gd center, six stem from hydroxyl groups, two from H_2O molecules, and one from an SO_4^{2-} tetrahedron, while in $Gd_2(OH)_4SO_4$, six are from hydroxyl groups and three from the SO_4^{2-} anion, although the $[GdO_9]$ unit is a tricapped trigonal prism in both structures; 3) $Gd_2(OH)_4SO_4$ shows a smaller gallery height ($\approx$6.85 Å) and cell volume ($\approx$314.97 Å^3) than $Gd_2(OH)_4SO_4{\cdot}2H_2O$ (gallery height $\approx$8.32 Å; cell volume $\approx$388.14 Å^3)[42] due to the absence of water of crystallization.

Field-emission (FE) SEM images showed that $Gd_2(OH)_4SO_4$ LRH crystallized as quasi-hexagons with lateral sizes and thicknesses of up to about 10 and 1.5 μm, respectively (Figure 4a). The selected-area electron diffraction (SAED) pattern (Figure 4c) of the crushed crystallites (Figure 4b) showed well-arranged diffraction spots indicating high crystallinity of the sample. The identified $(\bar{3}\bar{1}1)$, $(\bar{1}14)$, and $(\bar{4}05)$ peaks have d spacings of about 2.78, 1.47, and 1.23 Å, respectively, which are in close vicinity to the values of $d_{(\bar{3}\bar{1}1)}=2.694$, $d_{(\bar{1}14)}=1.442$, and $d_{(\bar{4}05)}=1.231$ Å derived from Rietveld refinement of the XRD pattern (Table S2 in the Supporting Information). The $(\bar{3}\bar{1}1)$ and $(\bar{1}14)$ planes would have a dihedral angle of about 84.7°, as calculated from the lattice constants and axis angle β derived by Rietveld refinement (Table 1), and the value is indeed close to that of about 80.3° obtained from the SAED pattern. HRTEM analysis (Figure 4d) resolved the lattice fringes well with interplanar distances of about 3.07 and 2.88 Å and a dihedral angle of about 87.3°, which can be assigned to the (002) and (310) planes of monoclinic $Gd_2(OH)_4SO_4$, respectively, according to the results of Rietveld refinement ($d_{(002)}=3.103$ Å and $d_{(310)}=2.855$ Å in Table S2 of the Supporting Information; calculated dihedral angle: $\approx$84.1°). The good correspondence of TEM analysis and Rietveld refinement further confirmed the crystal structure proposed in this work for the anhydrous LRH $Gd_2(OH)_4SO_4$.

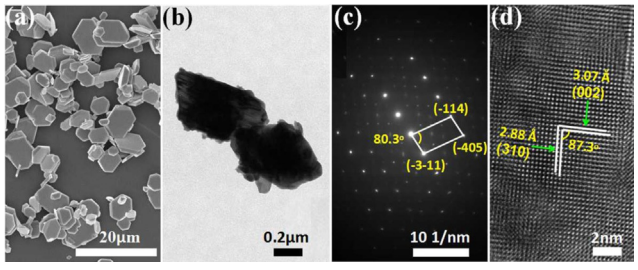

Figure 4. FESEM (a) and TEM (b) morphologies, SAED pattern (c), and HRTEM lattice fringes (d) for $Gd_2(OH)_4SO_4$.

Extended synthesis of anhydrous LRHs $Ln_2(OH)_4SO_4$

Under identical hydrothermal conditions of 150 °C and pH 10 for 24 h, the synthesis of $Ln_2(OH)_4SO_4$ anhydrous LRHs was attempted for the full spectrum of lanthanides, and Figure 5 shows the XRD patterns of a series of representative products. Only $Eu_2(OH)_4SO_4$ could be obtained aside from the $Gd_2(OH)_4SO_4$ discussed above. The La–Sm products conform well to the hydrated LRH $Ln_2(OH)_4SO_4{\cdot}2H_2O$.[29–31] Tb^{3+} (0.1095 nm for CN = 9) is only slightly smaller than Gd^{3+} (0.1107 nm for CN = 9), but its product crystallized as $Tb_2(OH)_5A{\cdot}nH_2O$,[15,32] instead of $Tb_2(OH)_4SO_4$, in which A was inferred to be SO_4^{2-} from the FTIR spectrum of the product (Figure S1 in the Supporting Information). The Er product exhibits amorphous diffraction and appears to be a transient state between those of Tb and Lu, as similarly observed before

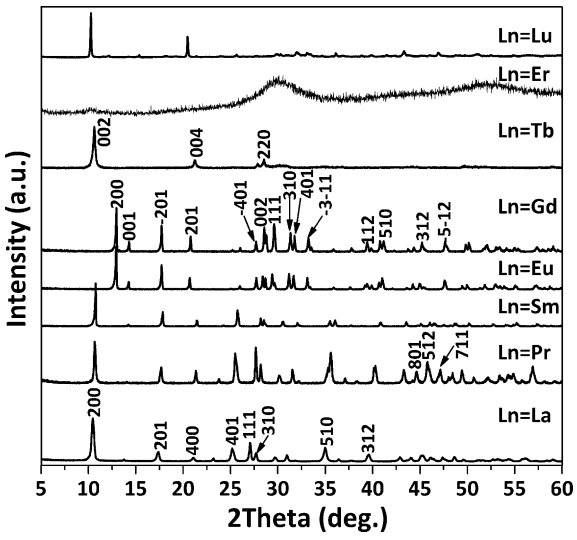

Figure 5. XRD patterns of the products obtained by hydrothermal reaction at 150 °C and pH 10.

during hydrothermal crystallization of $Ln_2(OH)_4SO_4{\cdot}2H_2O$ hydrated LRHs.[42] The Lu product cannot be indexed to any currently available JCPDS Card or literature reference. The results of elemental analysis (Table S3 in the Supporting Information) and FTIR spectroscopy (Figure S1 in the Supporting Information), however, indicated that it contains OH^- and SO_4^{2-} and has the nominal composition $Lu_2(OH)_{4.95}(SO_4)_{0.38}(NO_3)_{0.14}(CO_3)_{0.08}{\cdot}1.04H_2O$, which is quite close to that of the aforementioned $Tb_2(OH)_5(SO_4)_{0.5}{\cdot}nH_2O$. Structure determination is yet unsuccessful for this Lu product. The different crystallization behaviors across the lanthanide series were believed to be mainly caused by the lanthanide contraction. The Ln^{3+} ion in aqueous solution would be present as $[Ln(OH)_x(H_2O)_y(SO_4)_z]^{3-x-2z}$,[50] whereby the OH^-, SO_4^{2-}, and H_2O species are expected to compete with each other to coordinate with Ln^{3+} and thus affect the final composition of the product. Under the same hydrothermal conditions, the smaller ions of Tb–Lu would undergo a greater extent of hydrolysis (larger x and smaller z),[51] and therefore higher OH^-/Ln^{3+} molar ratios ($\approx$2.5) were observed for their products.

It can thus be inferred from the above that lowering the pH of the reaction system would favor the crystallization of $Ln_2(OH)_4SO_4$ anhydrous LRHs, and indeed phase-pure $Tb_2(OH)_4SO_4$ and $Dy_2(OH)_4SO_4$ were successfully produced at 150 °C and pH 9 and 8, respectively. Further lowering the pH to 7 allowed the crystallization of $Ln_2(OH)_4SO_4$ at 150 °C for the smaller ions Ho^{3+} (0.1072 nm for CN = 9), Y^{3+} (0.1075 nm for CN = 9), and Er^{3+} (0.1062 nm for CN = 9). At the lowest applicable pH of 7 (no precipitation at even lower pH), phase-pure $Ln_2(OH)_4SO_4$ can be successfully synthesized at a slightly higher temperature of 180 °C for the even smaller Tm^{3+} (0.1052 nm for CN = 9) and Yb^{3+} (0.1042 nm for CN = 9) and at 200 °C for the smallest Lu^{3+} (0.1032 nm for CN = 9). The XRD patterns of these extended members of the $Ln_2(OH)_4SO_4$ (Ln = Tb–Lu) family are shown in Figure 6, and their chemical compositions were further confirmed by the results of FTIR spectroscopy (Figure S3 in the Supporting Information) and elemental analysis (Table S4 in the Supporting Information, for Ln = Y, Lu). Our extensive synthetic efforts indicated that anhydrous LRHs $Ln_2(OH)_4SO_4$ are only obtainable for Ln = Eu–Lu (including Y). For the larger Ln ions La^{3+}–Sm^{3+}, either raising the reaction temperature or lowering the solution pH would lead to the crystallization of anhydrous $Ln(OH)SO_4$ (molar SO_4/Ln = 1:1). The above results thus clearly reveal that solution pH and reaction temperature decisively determine phase selection, and the optimal hydrothermal conditions vary with the type of Ln^{3+} owing to the different hydrolysis behaviors of Ln^{3+} due to the lanthanide contraction. It can also be inferred from the above results that either a lower pH or a higher reaction temperature facilitates coordination of SO_4^{2-} to Ln^{3+} and expels the weakest-coordinating H_2O molecules from the coordination sphere of Ln^{3+} to yield anhydrous $Ln_2(OH)_4SO_4$.

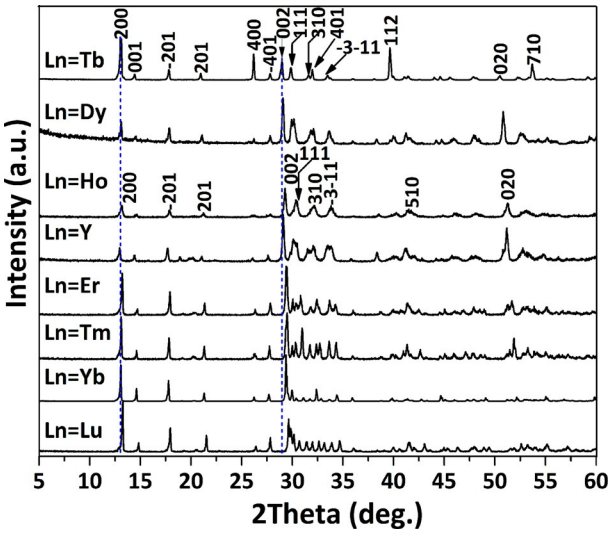

Figure 6. XRD patterns of the extended members of the $Ln_2(OH)_4SO_4$ (Ln = Tb–Lu and Y) family, the hydrothermal conditions of which are summarized in Table S5 of the Supporting Information.

SEM images (Figure S4 in the Supporting Information) revealed that the morphology of $Ln_2(OH)_4SO_4$ depends on the type of Ln and the hydrothermal conditions. The Eu, Gd, and Tb products, synthesized at relatively high pH values of 10 and 9, form quasi-hexagonal microplates (Figure S4 in the Supporting Information), whereas the Dy–Lu products, obtained at lower pH values of 8 and 7, form aggregated microspheres or irregular shapes (Figure S4 in the Supporting Information). The aggregation at lower pH was believed to be caused by attraction of the negatively charged SO_4^{2-} groups by surface adsorbed protons. The different morphologies and dimensions of the particles/crystallites may largely account for the varying relative intensities of XRD peaks, for example, (200) and (002), for different Ln (Figure 6).

With the structure model solved for $Gd_2(OH)_4SO_4$, the cell parameters of $Ln_2(OH)_4SO_4$ were derived by pattern fitting, and the results are tabulated in Table S6 of the Supporting Information and shown in Figure 7 as a function of the ionic radius of Ln^{3+}. The lattice constants (a, b, and c; Figure 7a–c) and cell volume (V; Figure 7d) tend to successively decrease for smaller Ln^{3+}, in accordance with lanthanide contraction, whereas the axis angle β behaves oppositely (Figure 7e). The b and c parameters show slopes of 1.625 and 1.052 with decreasing Ln^{3+} size from Eu^{3+} to Lu^{3+}, respectively, while the a parameter declines to a much lesser extent and with a slope of only 0.395. The (0kl) and (h00) diffractions reflect structural features of the host layers and the stacking of the host layer along the a axis, respectively. Shrinkage of the a dimension is thus significantly constrained by the rigid SO_4^{2-} pillars because the interlayer SO_4^{2-} rarely shows substantial distortion from the regular tetrahedron in most crystal structures. The limited contraction of the a parameter corresponds well with the almost nonshifting (h00) peaks (e.g., 200; Figure 6).

Thermolysis

The thermal decomposition of $Ln_2(OH)_4SO_4$ (Ln = Eu-Lu, and Y) was investigated by thermogravimetric/differential thermal analysis (TG/DTA) in simulated air in the temperature range from RT to 1560 °C. The results for $Eu_2(OH)_4SO_4$ are shown in Figure 8a, and the rest can be found in Figure S5 of the Sup-

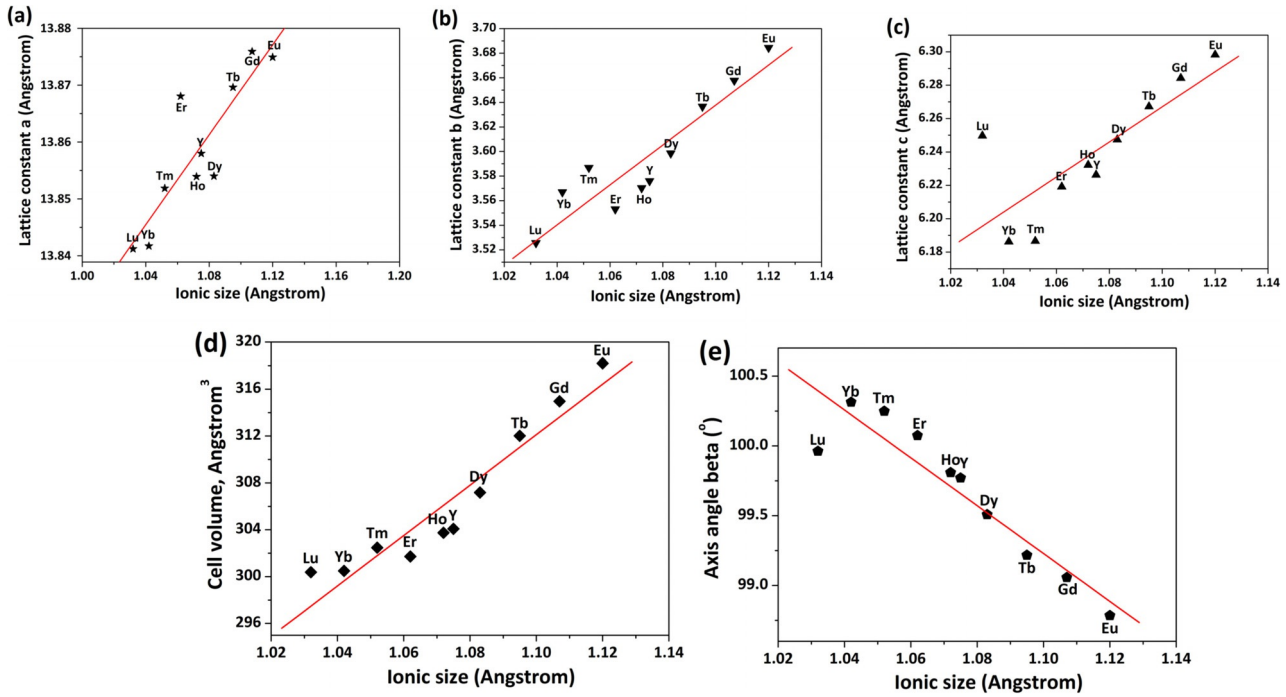

Figure 7. Correlation of lattice parameters *a* (a), *b* (b), and *c* (c), cell volume *V* (d), and axis angle β (e) with the ionic radius of Ln^{3+} for $Ln_2(OH)_4SO_4$ (Ln = Eu–Lu, Y). The ionic radii for nine-coordinate Ln^{3+} are cited from ref.[53].

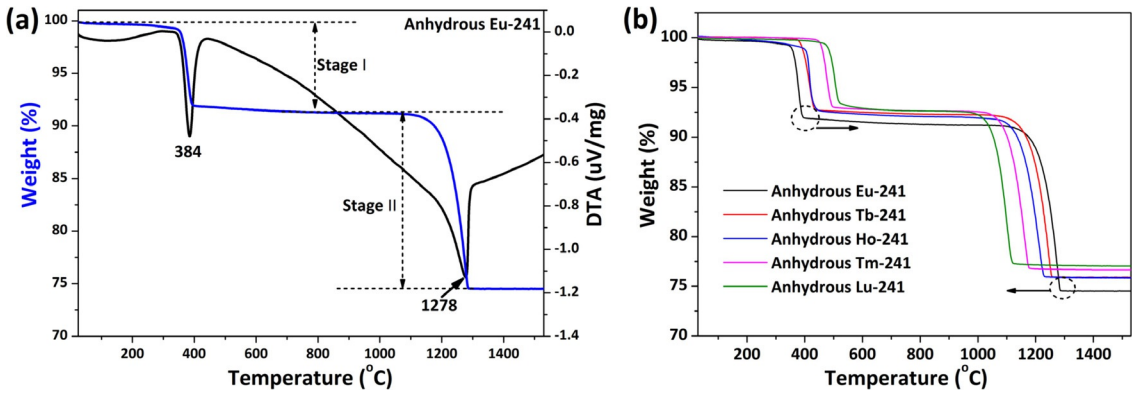

Figure 8. TG/DTA curves for $Eu_2(OH)_4SO_4$ (a) and comparison of the TG curves for some representative anhydrous $Ln_2(OH)_4SO_4$ compounds (b).

porting Information. Compared with its hydrated $Eu(OH)_4SO_4{\cdot}2H_2O$ counterpart (Figure S6 in the Supporting Information), a distinct feature of $Eu_2(OH)_4SO_4$ is that it lacks the stage of dehydration up to about 300 °C (≈7.7% of weight loss accompanied by an endotherm at ≈269 °C; Figure S6 in the Supporting Information), which again confirms the anhydrous nature of $Eu_2(OH)_4SO_4$. The $Ln_2(OH)_4SO_4$ compounds synthesized in this work similarly show two steps of weight loss that correspond to dehydroxylation (up to ≈550 °C) and desulfurization (above ≈1000 °C) to yield $Ln_2O_2SO_4$ and Ln_2O_3, respectively (Figure 8). The reactions of the two stages can accordingly be expressed as $Ln_2(OH)_4SO_4 \rightarrow Ln_2O_2SO_4 + 2H_2O$ (stage I) and $Ln_2O_2SO_4 \rightarrow Ln_2O_3 + SO_3$ (stage II). The good correspondence of the observed (Table 3) and theoretical (Table S7 in the Support-

Table 3. Data for thermal decomposition of $Ln_2(OH)_4SO_4$ anhydrous LRHs in simulated air (Ln = Eu–Lu, Y).

Ln	Peak 1 [°C]	Peak 2 [°C]	*T* range for $Ln_2O_2SO_4$ [°C]	Weight loss I [%]	Weight loss II [%]
Eu	384	1278	437–1125	8.62	16.93
Gd	415	1270	471–1123	8.16	16.71
Tb	422	1249	479–1086	7.62	16.51
Dy	450	1264	505–1098	7.71	16.57
Ho	420	1215	491–1066	7.84	16.31
Y	430	1208	503–1057	11.27	23.50
Er	461	1192	523–1051	8.93	16.07
Tm	483	1167	539–1024	7.24	16.09
Yb	502	1118	557–980	7.11	15.69
Lu	508	1104	565–978	7.32	15.61

ing Information) weight losses of each stage further confirm the proposed decomposition process. The temperature at which each stage occurs nonetheless shows clear dependence on the type of Ln. As shown in Figure 8b and Table 3, dehydroxylation occurs at higher temperature for smaller Ln^{3+}, whereas desulfurization behaves oppositely. The temperature range of $Ln_2O_2SO_4$ existence is thus narrower for smaller Ln^{3+}, which makes $Lu_2O_2SO_4$ the least stable among the $Ln_2O_2SO_4$ family.

Green synthesis of $Ln_2O_2SO_4$ and Ln_2O_2S

According to the results of TGA (Figure 8b), calcining $Ln_2(OH)_4SO_4$ in air at 800 °C for 1 h yielded $Ln_2O_2SO_4$ in phase-pure form (Figure S7). The group of oxide sulfate compounds crystallizes in the monoclinic system (space group *C*2/*c*). Each Ln atom is bonded with seven oxygen atoms (three from SO_4^{2-}) to form a mono-capped trigonal prism.[31] The diffraction peaks of $Ln_2O_2SO_4$ clearly shift to larger 2θ values for smaller Ln^{3+}, in compliance with lanthanide contraction. The $Ln_2(OH)_4SO_4$ (Ln = Eu–Lu, Y) anhydrous LRHs newly discovered in this work, together with the $Ln_2(OH)_4SO_4{\cdot}2H_2O$ hydrated LRH reported recently (Ln = La–Dy),[42] allow for the first time the green synthesis of $Ln_2(OH)_4SO_4$ for the full spectrum of lanthanides (excluding Ce^{3+} and Pm^{3+}). Figure 9 shows structural parameters of the $Ln_2O_2SO_4$ derived from $Ln_2(OH)_4SO_4$ (Ln = Eu–Lu, Y) and $Ln_2(OH)_4SO_4{\cdot}2H_2O$ (Ln = La–Sm).[42] The lattice constants (Figure 9a–c) and cell volume (Figure 9d) linearly decrease for smaller Ln^{3+}, whereas the opposite trend was observed for the axis angle β (Figure 9e).

Treating $Ln_2(OH)_4SO_4$ in hydrogen may allow dehydroxylation and reduction of S^{6+} in SO_4^{2-} to S^{2-} and thus the formation of Ln_2O_2S. Considering that the reducing power of H_2 is still rather low at the dehydration temperature (up to ≈550 °C, Figure 8b), Ln_2O_2S was expected to form by the sequential reactions $Ln_2(OH)_4SO_4 \rightarrow Ln_2O_2SO_4 + 2H_2O$ (dehydroxylation) and $Ln_2O_2SO_4 + 4H_2 \rightarrow Ln_2O_2S + 4H_2O$ (reduction). The XRD patterns of the products from calcination of $Ln_2(OH)_4SO_4$ in flowing H_2 at 1200 °C for 1 h are shown in Figure S8 of the Supporting Information. The Eu and Gd products can be well indexed to single-phase Ln_2O_2S of hexagonal structure. The oxide sulfide compounds crystallize in space group $P\bar{3}m1$, whereby Ln is bonded with three sulfur and four oxygen atoms in a mono-capped polyhedron with sevenfold coordination.[31] Cubic-structured Ln_2O_3 impurity was unexpectedly found for the products of smaller Ln^{3+} (Ln = Tb–Eu, Y), as indicated by an asterisk for the (222) diffraction peak in each case. Rietveld refinement showed that the fraction of Ln_2O_3 gradually increases with decreasing size of Ln^{3+}, from about 3.3 wt% for Tb^{3+} to about 78.5 wt% for Lu^{3+}. The phase constituents and cell parameters determined by Rietveld analysis for Ln_2O_2S and Ln_2O_3 can be found in Table S8 of the Supporting Information. Calcining $Ln_2(OH)_4SO_4$ at the lower temperature of 900 °C, at which the reducing powder of H_2 is known to be acceptable and $Ln_2O_2SO_4$ would be stable in air, yielded similar XRD results (Figure 8b and Table 3). The above observations may thus reveal that the affinity of SO_4^{2-} towards Ln^{3+} is significantly lower in H_2 than in air. As a result, S could have partially been converted to SO_x on calcining the $Ln_2(OH)_4SO_4$ of Ln = Tb–Lu (including Y) in H_2. The gradually decreasing thermal stability

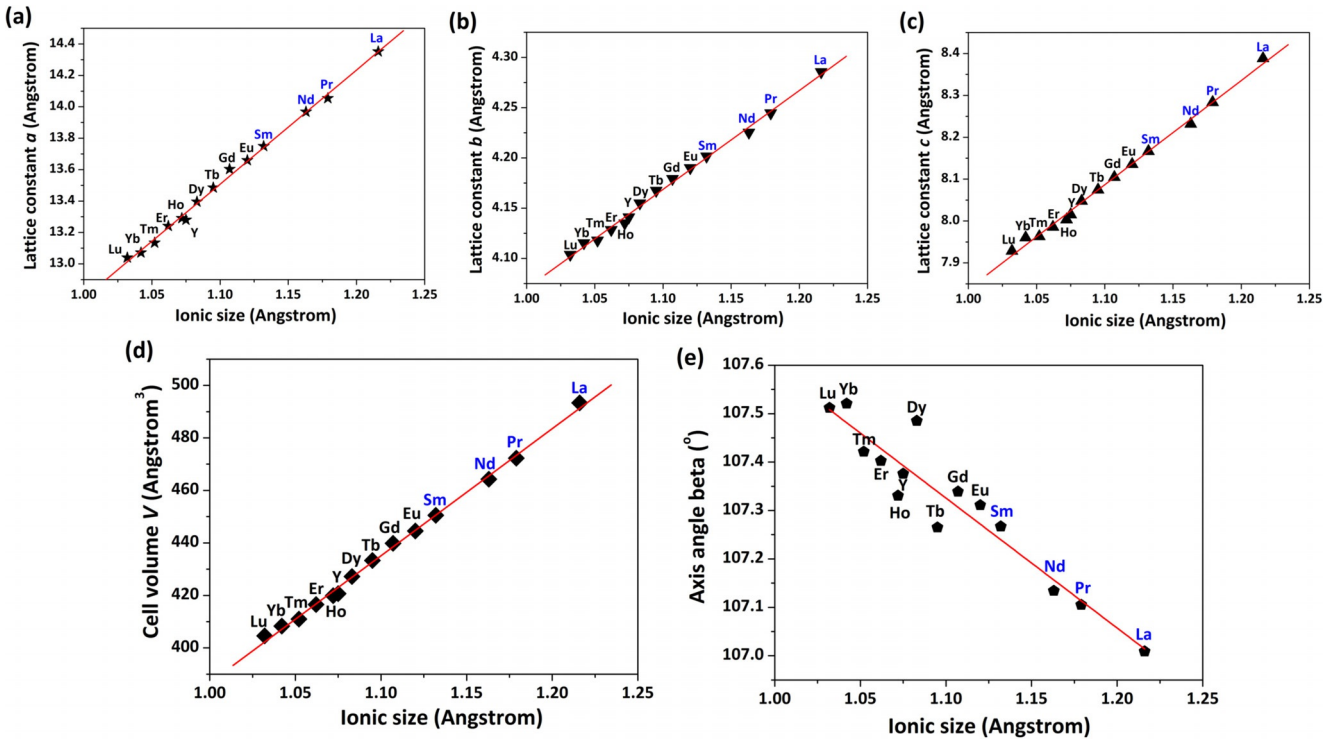

Figure 9. Correlation of lattice parameters *a* (a), *b* (b), and *c* (c), cell volume *V* (d), and axis angle β (e) with the ionic radius of Ln^{3+} for $Ln_2O_2SO_4$. The ionic radius of Ln^{3+} and the structural data for Ln = La–Sm (blue) are taken from refs. [52, 42], respectively.

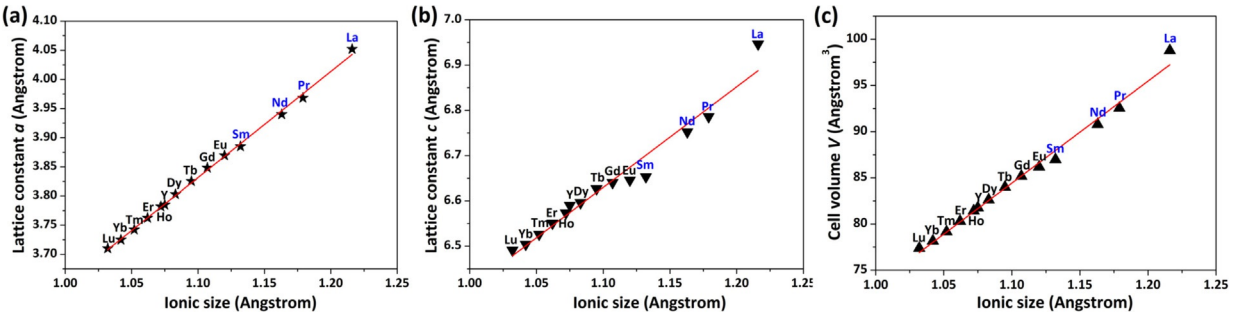

Figure 10. Correlation of the lattice parameters *a* (a) and *c* (b) and cell volume *V* (c) with the ionic radius of Ln^{3+} for Ln_2O_2S. The ionic radius of Ln^{3+} and the structural data for Ln = La–Sm are taken from refs. [52, 42], respectively.

of $Ln_2O_2SO_4$ (Figure 8b and Table 3) well explains the increasing content of Ln_2O_3 in the reduction product for smaller Ln^{3+} (Table S8 in the Supporting Information). Figure 10 shows the influence of Ln^{3+} size on the structural parameters of Ln_2O_2S for the full spectrum of lanthanides. The lattice constants (*a* and *c*, Figure 10a and b) and cell volume (Figure 10c) decrease almost linearly with decreasing size of Ln^{3+}.

Photoluminescence

Photoluminescence (PL) studies indicated that the $Eu_2(OH)_4SO_4$ and $Tb_2(OH)_4SO_4$ LRH compounds produce red and green emissions through their characteristic f–f transitions under UV excitation, and the excitation (PLE) and emission (PL) spectra are shown in Figure 11. It is noteworthy that the other optically active ions of Gd^{3+}, Dy^{3+}, Ho^{3+}, Er^{3+}, and Tm^{3+} exhibit negligible luminescence in the $Ln_2(OH)_4SO_4$ lattice. The PLE spectrum of $Eu_2(OH)_4SO_4$ (λ_{em} = 617 nm) shows sharp excitation peaks ascribable to the intra-$4f^6$ transitions of Eu^{3+}, of which the $^7F_0 \rightarrow {}^5L_6$ transition at 395 nm is the strongest (Figure 11a). Under excitation at 395 nm, the $^5D_0 \rightarrow {}^7F_J$ transitions of Eu^{3+} were observed, of which the $^5D_0 \rightarrow {}^7F_2$ (617 nm) red emission is the most prominent (Figure 11a). This conforms to the low site symmetry of Eu^{3+} in the monoclinic lattice. The excitation spectrum of $Tb_2(OH)_4SO_4$ (λ_{em} = 545 nm) is composed of the $4f^8 \rightarrow 4f^75d^1$ inter-configurational transitions and the intra-$4f^8$ transitions in the spectral regions of about 200–300 and 300–400 nm, respectively, of which the former is dominant (Figure 11b). Under excitation of the spin-allowed f–d transition at 243 nm, the typical $^5D_4 \rightarrow {}^7F_J$ (J = 3–6) transitions of Tb^{3+} were produced, among which the $^5D_4 \rightarrow {}^7F_5$ green emission at 545 nm is predominant (Figure 11b). The fluorescence decay kinetics of the 617 nm red emission of $Eu_2(OH)_4SO_4$ (λ_{ex} = 395 nm) and the 545 nm green emission of $Tb_2(OH)_4SO_4$ (λ_{ex} = 243 nm) can both be fitted with a single exponential (Figure S9 in the Supporting Information), from which lifetimes of 0.67 and 0.78 ms were determined for the two compounds, respectively. The CIE chromaticity coordinates derived from the emission spectra are (0.60, 0.39) and (0.36, 0.55) for $Eu_2(OH)_4SO_4$ and $Tb_2(OH)_4SO_4$, corresponding to orange-red and yellowish green colors, respectively (Figure S10 in the Supporting Information).

Conclusion

The anhydrous hydroxide sulfates $Ln_2(OH)_4SO_4$ (Ln = Eu–Lu, Y) were synthesized as a new family of LRHs by manipulating the coordination of the Ln^{3+} ion. Detailed analyses of the compounds found that: 1) $Ln_2(OH)_4SO_4$ crystallizes in the monoclinic system (space group *C*2/*m*) with structures built up by alternate stacking of the interlayer SO_4^{2-} and the two-dimensional host layers composed of [LnO_9] polyhedra along the *a* axis.

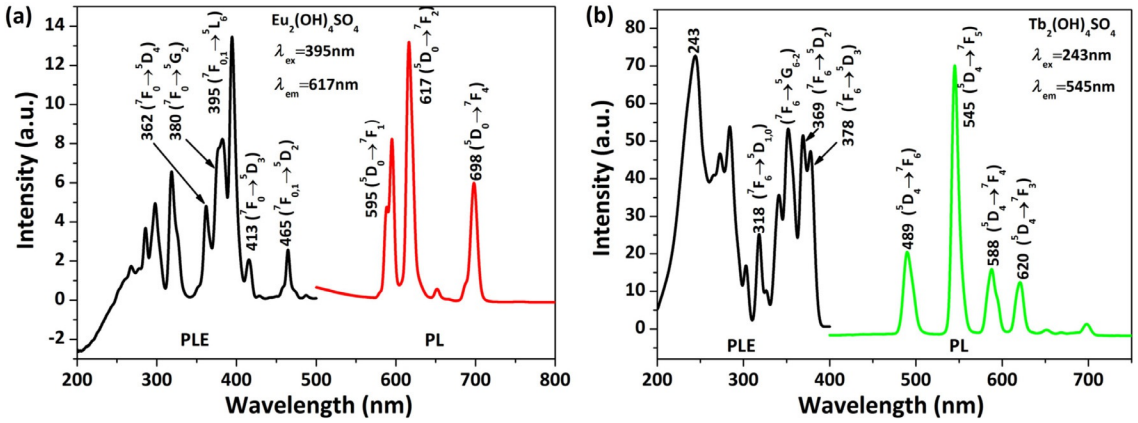

Figure 11. PLE (black lines) and PL (colored lines) spectra of $Eu_2(OH)_4SO_4$ (a) and $Tb_2(OH)_4SO_4$ (b).

The $[LnO_9]$ polyhedron is a tricapped trigonal prism and the host layers are linked together by edging sharing with the SO_4^{2-} tetrahedra. $Ln_2(OH)_4SO_4$ shows a smaller gallery height and cell volume than its hydrated counterpart $Ln_2(OH)_4SO_4{\cdot}2H_2O$ due to the absence of water of crystallization; 2) the lattice parameters (*a*, *b*, *c*) and cell volume tend to decrease with decreasing size of Ln^{3+}, while the axis angle β behaves oppositely. The *a* parameter shows significantly smaller contraction than the *b* and *c* parameters with decreasing Ln^{3+} size due to the rigid pillaring of interlayer SO_4^{2-}; 3) $Ln_2(OH)_4SO_4$ undergoes dehydroxylation and then desulfurization to yield $Ln_2O_2SO_4$ and finally Ln_2O_3 in air. The temperature window of $Ln_2O_2SO_4$ existence was found to decrease with decreasing size of Ln^{3+}; 4) calcining $Ln_2(OH)_4SO_4$ in air at 800 °C yielded single-phase monoclinic $Ln_2O_2SO_4$ for Ln = Eu–Lu (including Y); 5) $Eu_2(OH)_4SO_4$ and $Tb_2(OH)_4SO_4$ exhibit orange-red [chromaticity coordinates: (0.60, 0.39)] and yellowish green [chromaticity coordinates: (0.36, 0.55)] emissions under UV excitation at 395 and 243 nm, respectively. The 617 nm Eu^{3+} and 545 nm Tb^{3+} emissions have fluorescence lifetimes of 0.67 and 0.78 ms, respectively.

Experimental Section

Reagents and synthesis

$Ln(NO_3)_3{\cdot}6H_2O$ (Ln = La–Lu, Y, 99.99% pure), $(NH_4)_2SO_4$ (>99.5% pure), and $NH_3{\cdot}H_2O$ solution (ultrahigh purity) were purchased from Kanto Chemical Co. Inc. (Tokyo, Japan) and were used as received. Milli-Q filtered water (resistivity >18 MΩ cm) was used throughout the experiments. $Ln(NO_3)_3{\cdot}6H_2O$ were dissolved in water to make Ln^{3+} solutions of 0.1 mol L^{-1}. In a typical synthesis, 6 mmol of $(NH_4)_2SO_4$ particles (0.79284 g) were dissolved in 60 mL of the Ln^{3+} solution (6 mmol of Ln^{3+}), followed by dropwise addition of $NH_3{\cdot}H_2O$ for pH adjustment. The resultant turbid solution was homogenized at room temperature with magnetic stirring for 10 min before being transferred to a Teflon-lined stainless steel autoclave of 100 mL capacity for 24 h of hydrothermal crystallization in an air oven preheated to a predetermined temperature. The resultant solid was recovered by centrifugation after allowing the autoclave to cool to room temperature, washed with water three times and ethanol once, and then dried in air at 70 °C for 24 h.

Anhydrous $Ln_2(OH)_4SO_4$ was calcined in ambient air at 800 °C and in flowing H_2 (200 mL min^{-1}) at 900–1200 °C to produce $Ln_2O_2SO_4$ and Ln_2O_2S, respectively, with a holding time of 1 h at the annealing temperature and a heating rate of 5 °C min^{-1} in the ramp stage.

Characterization

Elemental contents of the products were determined for Ln by inductively coupled plasma (ICP) spectroscopy (Model IRIS Advantage, Jarrell-Ash Japan, Kyoto, Japan), for N by spectrophotometry (Ubest-35, Japan Spectroscopic Co., Ltd, Tokyo), and for C and S by combustion/IR absorption (Model CS-444LS, LECO, St. Joseph, MI). The detection limit of the above analyses is 0.01 wt% in each case. Phase characterization was performed by XRD (Model RIN T2200, Rigaku, Tokyo, Japan) at 40 kV/40 mA by using monochromatic $Cu_{K\alpha}$ radiation (λ = 0.15406 nm). The XRD data for Rietveld analysis were measured in step-scan mode with a step size of 0.02° and an accumulation time of 35 s. Profile fitting, crystal structure searching, and Rietveld refinements were performed with the TOPAS 4.2 software.[53] Product morphology was observed by FESEM under an acceleration voltage of 10 kV (Model S-5000, Hitachi, Tokyo). SAED and high-resolution lattice imaging were done with a transmission electron microscope working at 200 kV (TEM, Model JEM-2100F, JOEL, Tokyo). The TEM sample was prepared by dispersing a small amount of sufficiently ground powder in ethanol by sonication, followed by depositing a few drops of the resultant suspension onto a carbon-coated grid and then air drying. FTIR spectroscopy (Model 4200, JASCO, Tokyo), performed by the standard KBr pellet method, was used to investigate the functional groups in the compounds. Thermal decomposition of the layered compound was investigated by TG/DTA (Model STA449F3, Jupiter, NETZSCH, Germany) in flowing simulated air (50 mL min^{-1}) with a constant heating rate of 10 °C min^{-1} in the temperature range from RT to 1560 °C. The excitation, emission, and fluorescence decay kinetics were measured with an FP-6500 fluorospectrophotometer (JASCO, Tokyo) equipped with a 150 W xenon lamp for excitation, a scan speed of 100 nm min^{-1}, and a slit width of 3 nm for both excitation and emission.

Further details of the crystal structure of $Gd_2(OH)_4SO_4$, may be obtained from Fachinformationszentrum Karlsruhe, 76344 Eggenstein-Leopoldshafen, Germany (fax: (+49)7247-808-666; E-mail: crystdata@fiz-karlsruhe.de; http://www.fiz-karlsruhe.de/request for deposited data.html on quoting the deposition number: CSD-433211.

Acknowledgements

This work is supported in part by the National Natural Science Foundation of China (Grants Nos. 51702020, and 51672039), Doctoral Research Fund of Liaoning Province (Grant No. 20170520103) and the Russian Foundation for Basic Research (17-52-53031). X.W. acknowledges the financial support from the China Scholarship Council for her overseas Ph. D. study (Contract No. 201406080035).

Conflict of interest

The authors declare no conflict of interest.

Keywords: hydrothermal synthesis · layered compounds · luminescence · oxide sulfates · rare earths

[1] L. Junseok, K. Jinhwan, J. K. Won, *Chem. Mater.* **2016**, *28*, 6417–6424.
[2] W. P. Zhang, X. Y. Xiao, Y. Li, X. Y. Zeng, L. L. Zheng, C. X. Wan, *Appl. Surf. Sci.* **2016**, *389*, 496–506.
[3] Y. Gu, Z. Lu, Z. Chang, J. Liu, X. Lei, Y. Li, X. Sun, *J. Mater. Chem. A* **2013**, *1*, 10655–10661.
[4] J. Liu, G. M. Chen, J. P. Yang, *Polymer* **2008**, *49*, 3923–3927.
[5] Z. Q. Hu, G. M. Chen, *Adv. Mater.* **2014**, *26*, 5950–5956.
[6] T. C. Cao, K. L. Xu, G. M. Chen, C.-Y. Guo, *RSC Adv.* **2013**, *3*, 6282–6285.
[7] Z. Zhang, G. M. Chen, J. G. Liu, *RSC Adv.* **2014**, *4*, 7991–7997.
[8] F. Gándara, J. Perles, N. Snejko, M. Iglesias, B. Gomez-Lor, E. Gutierrez-Puebla, M. A. Monge, *Angew. Chem. Int. Ed.* **2006**, *45*, 7998–8001; *Angew. Chem.* **2006**, *118*, 8166–8169.
[9] L. J. McIntyre, L. K. Jackson, A. M. Fogg, *Chem. Mater.* **2008**, *20*, 335–340.
[10] L. J. McIntyre, T. J. Prior, A. M. Fogg, *Chem. Mater.* **2010**, *22*, 2635–2645.
[11] Y. X. Song, M. Luo, C. S. Lin, N. Ye, *Chem. Mater.* **2017**, *29*, 896–903.
[12] F. L. Carter, S. Levinson, *Inorg. Chem.* **1969**, *8*, 2788–2791.

[13] J. M. Haschke, *Inorg. Chem.* **1974**, *13*, 1812 – 1818.
[14] A. D. Yapryntsev, A. E. Baranchikov, L. S. Skogareva, A. E. Goldt, I. P. Stolyarov, O. S. Ivanova, V. V. Kozik, V. K. Ivanov, *CrystEngComm* **2015**, *17*, 2667 – 2674.
[15] X. L. Wu, J.-G. Li, Q. Zhu, W. G. Liu, J. Li, X. D. Li, X. D. Sun, Y. Sakka, *J. Mater. Chem. C* **2015**, *3*, 3428 – 3437.
[16] H. Kim, B. I. Lee, H. Jeong, S. H. Byeon, *J. Mater. Chem. C* **2015**, *3*, 7437 – 7445.
[17] L. J. McIntyre, L. K. Jackson, A. M. Fogg, *J. Phys. Chem. Solids* **2008**, *69*, 1070 – 1074.
[18] F. X. Geng, Y. Matsushita, R. Z. Ma, H. Xin, M. Tanaka, F. Izumi, N. Iyi, T. Sasaki, *J. Am. Chem. Soc.* **2008**, *130*, 16344 – 16350.
[19] L. Poudret, T. J. Prior, L. J. McIntyre, A. M. Fogg, *Chem. Mater.* **2008**, *20*, 7447 – 7453.
[20] F. X. Geng, H. Xin, Y. Matsushita, R. Z. Ma, M. Tanaka, F. Izumi, N. Iyi, T. Sasaki, *Chem. Eur. J.* **2008**, *14*, 9255 – 9260.
[21] Q. Zhu, J.-G. Li, X. D. Li, X. D. Sun, Y. Qi, M. Y. Zhu, Y. Sakka, *Sci. Technol. Adv. Mater.* **2014**, *15*, 014203.
[22] S. A. Hindocha, L. J. McIntyre, A. M. Fogg, *J. Solid State Chem.* **2009**, *182*, 1070 – 1074.
[23] L. L. Liu, M. H. Yu, J. Zhang, B. K. Wang, W. S. Liu, Y. Tang, *J. Mater. Chem. C* **2015**, *3*, 2326 – 2333.
[24] H. J. Jeong, B.-I. Lee, S.-H. Byeon, *ACS Appl. Mater. Interfaces* **2016**, *8*, 10946 – 10953.
[25] Y. Xiang, X.-F. Yu, D.-F. He, Z. B. Sun, Z. J. Cao, Q.-Q. Wang, *Adv. Funct. Mater.* **2011**, *21*, 4388 – 4396.
[26] F. X. Geng, Y. Matsushita, R. Z. Ma, H. Xin, M. Tanaka, N. Iyi, T. Sasaki, *Inorg. Chem.* **2009**, *48*, 6724 – 6730.
[27] K.-H. Lee, S.-H. Byeon, *Eur. J. Inorg. Chem.* **2009**, *7*, 929 – 936.
[28] K.-H. Lee, S.-H. Byeon, *Eur. J. Inorg. Chem.* **2009**, *31*, 4727 – 4732.
[29] J. B. Liang, R. Z. Ma, F. X. Geng, Y. Ebina, T. Sasaki, *Chem. Mater.* **2010**, *22*, 6001 – 6007.
[30] F. X. Geng, R. Z. Ma, Y. Matsushita, J. B. Liang, Y. Michiue, T. Sasaki, *Inorg. Chem.* **2011**, *50*, 6667 – 6672.
[31] X. J. Wang, J.-G. Li, M. S. Molokeev, Q. Zhu, X. D. Li, X. D. Sun, *Chem. Eng. J.* **2016**, *302*, 577 – 586.
[32] X. J. Wang, J.-G. Li, Q. Zhu, X. D. Sun, *J. Am. Ceram. Soc.* **2015**, *98*, 3236 – 3242.
[33] Q. Zhu, J.-G. Li, C. Y. Zhi, R. Z. Ma, T. Sasaki, J. X. Xu, C. H. Liu, X. D. Li, X. D. Sun, Y. Sakka, *J. Mater. Chem.* **2011**, *21*, 6903 – 6908.
[34] C. F. Guo, L. Luan, C. H. Chen, D. X. Huang, Q. Su, *Mater. Lett.* **2008**, *62*, 600 – 602.
[35] C.-C. Kang, R.-S. Liu, J.-C. Chang, B.-J. Lee, *Chem. Mater.* **2003**, *15*, 3966 – 3968.
[36] A. G. Ali, B. F. Dejene, H. C. Swart, *Physica B* **2016**, *480*, 174 – 180
[37] C. R. Ronda, G. Zeitler, H. Schreinemacher, N. Conrads, D. U. Wiechert, Koninklijke Phillips Electronics, *N*-V-, Eindhoven (NL), United States US 2011/0114887 A1.
[38] S. Tan, S. N. Paglieri, D. M. Li, *Catal. Commun.* **2016**, *73*, 16 – 21.
[39] D. J. Zhang, F. Yoshioka, K. Ikeue, M. Machida, *Chem. Mater.* **2008**, *20*, 6697 – 6703.
[40] F. S. Chen, G. Chen, T. Liu, N. Zhang, X. H. Liu, H. M. Luo, J. H. Li, L. M. Chen, R. Z. Ma, G. Z. Qiu, *Sci. Rep.* **2015**, *5*, 17934.
[41] J. B. Lian, F. Liu, X. J. Wang, X. D. Sun, *Powder Technol.* **2014**, *253*, 187 – 192.
[42] X. J. Wang, J.-G. Li, M. S. Molokeev, X. J. Wang, W. G. Liu, Q. Zhu, H. Tanaka, K. Suzuta, B.-N. Kim, Y. Sakka, *RSC Adv.* **2017**, *7*, 13331 – 13339.
[43] N. N. Golovnev, M. S. Molokeev, S. N. Vereshchagin, V. V. Atuchin, *J. Coord. Chem.* **2015**, *68*, 1865 – 1877.
[44] V. Favre-Nicolin, C. R. Fox, *Mater. Sci. Forum* **2004**, *443 – 444*, 35 – 38.
[45] V. Favre-Nicolin, C. R. Fox, *J. Appl. Crystallogr.* **2002**, *35*, 734 – 743.
[46] Z. G. Xia, M. S. Molokeev, A. S. Oreshonkov, V. V. Atuchin, R.-S. Liu, C. Dong, *Phys. Chem. Chem. Phys.* **2014**, *16*, 5952 – 5957.
[47] I. D. Brown, D. Altermatt, *Acta Crystallogr. Sect. B* **1985**, *41*, 244 – 247.
[48] N. E. Brese, M. O'Keeffe, *Acta Crystallogr. Sect. B* **1991**, *47*, 192 – 197.
[49] A. L. Spek, *J. Appl. Crystallogr.* **2003**, *36*, 7 – 13.
[50] L. C. Thompson, *Complexes, in Handbook on the Physics and Chemistry of Rare Earths*, (Eds.: K. A. Gschneidner, Jr., L. Eyring), North-Holland Physics, Amsterdam, **1979**.
[51] E. N. Rizkalla, G. R. Choppin, *J. Alloys Compd.* **1992**, *180*, 325 – 336.
[52] R. D. Shannon, *Acta Crystallogr. Sect. A* **1976**, *32*, 751 – 767.
[53] Bruker AXS TOPAS V4: General profile and structure analysis software for powder diffraction data.- User's manual, Bruker AXS, Karlsruhe, Germany (2008).

Manuscript received: July 15, 2017
Accepted manuscript online: September 7, 2017
Version of record online: October 23, 2017